High-efficiency Ultrathin Nonlocal Waterborne Acoustic Metasurface

Hong-Tao Zhou,[1] Wen-Xiao Fu,[1] Yan-Feng Wang,[1,*] and Yue-Sheng Wang[1,2,†]

[1] *Department of Mechanics, School of Mechanical Engineering, Tianjin University, Tianjin 300350, China*
[2] *Department of Mechanics, Beijing Jiaotong University, Beijing 100044, China*

(Received 28 December 2020; revised 1 March 2021; accepted 30 March 2021; published 28 April 2021)

High-performance and lightweight waterborne acoustic devices have provided important support for the development of ocean exploration, health monitoring, etc. In this work, we propose a high-efficiency ultrathin nonlocal waterborne acoustic metasurface. Due to strong nonlocal interaction between the waterborne unit cells induced by the fluid-solid interaction, a nonlocal design concept based on diffraction theory and the optimization approach is proposed to design waterborne acoustic metasurfaces, in contrast to the local design based on the generalized Snell's law. The theoretical efficiency limitation of the generalized Snell's law can be broken, and unitary efficiency could be obtained even for large-angle anomalous reflection. The high-efficiency modulation is achieved owing to the energy flow along the metasurface resulting from the nonlocal interaction. The thickness of the waterborne acoustic metasurface can be minimized to one tenth or even one sixtieth of the working wavelength. The nonlocal design with fluid-solid interaction paves the way for high-efficiency and deep-subwavelength waterborne acoustic wave manipulation.

DOI: 10.1103/PhysRevApplied.15.044046

I. INTRODUCTION

As one kind of artificial subwavelength microstructure, acoustic metasurfaces [1–4] have witnessed rapid development in manipulating acoustic wave propagation. In recent years, waterborne acoustic wave manipulation has received extensive interest [5–14]. Based on the generalized Snell's law (GSL) [1,15], different extraordinary functions have been successively achieved [5–9,12–14], such as conversion from cylindrical waves to plane waves [5,7], beam steering [5,12], focusing [9,13,14], carpet cloaking [9,14], etc. However, these waterborne acoustic metasurfaces (WAM) based only on local phase gradient modulation cannot fully control the propagation direction of acoustic waves [16,17]. Therefore, their efficiencies are mostly subject to the inherent limitation of the GSL [16,17]. In particular, the efficiency decreases sharply with the increase in the reflection angle for anomalous reflection, due to the impedance mismatch between the incident and reflected waves [16,17]. Hence, improvements in the efficiency of the WAMs are expected, especially for large-angle reflection.

Actually, many methods [16–25] have been proposed to enhance the efficiency of airborne acoustic metasurfaces. Based on the impedance-matched theory, scattering-free anomalous reflection and refraction have been successively achieved [16,17]. With independent amplitude and phase modulations, high-quality and high-fidelity airborne acoustic holograms were generated using lossy unit cells [19,24]. By considering the nonlocality between unit cells, unitary efficiency of extreme beam steering was achieved using passive metastructures with balanced gain and loss distributions [18]. In particular, diffraction theory [20–23,25,26] was applied to independently control the amplitudes of different diffraction components. Nearly perfect energy conversion is fulfilled by various acoustic metagratings, such as surface grooves with nonlocal coupling [20,21,26], C-shaped meta-atoms with Willis coupling [23], binary cells with empty walls and coiling-up structures [25], zigzag microstructures with integer parity [22], etc. In general, these high-efficiency metasurfaces require a nonlocal response with energy flowing along the surface [16,18,21,27].

Recently, acoustic metagratings have been extended to underwater acoustic wave manipulation [10,11]. Ultrasound underwater carpet cloaking was realized by a metagrating with simple grooves [10]. Beam splitting and asymmetric transmission were achieved by a metagrating with iron cylinders [11]. Although high-efficiency manipulation can be obtained, the thickness of underwater metagratings may exceed half of the operating wavelength [10,11]. Therefore, it is still a challenge to design ultrathin WAMs with high-efficiency manipulation.

In addition, waterborne and airborne acoustic metasurfaces are distinctly different due to the high impedance contrast of water and air [28]. The interface between the solid and air is usually considered to be rigid for airborne

*wangyanfeng@tju.edu.cn
†yswang@tju.edu.cn

 © 2021 American Physical Society

acoustic metasurfaces [3,11]. This guarantees that the unit cells do not affect each other. Thus, the phase shift of a unit cell in the metasurface can be well predicted by considering a single unit cell [3]. This allows on-demand wavefront manipulation by assembling unit cells with various phase profiles. The local design strategy based on the GSL is widely applied for airborne acoustic metasurfaces [1,2]. However, the fluid-solid interaction (FSI) cannot be neglected for WAMs [28–30]. The prescribed reflection wavefronts may be obviously distorted if the solid material is replaced with a rigid one [11], owing to the coupling of acoustic and elastic waves through the FSI [29,31]. Therefore, the local design may be not practicable for WAMs, and the effect of the FSI should be further explored.

In this work, we develop a nonlocal design of a high-efficiency ultrathin WAM by combining diffraction theory and an optimization method. Similar to airborne acoustic metasurfaces, we start with a WAM for anomalous reflection according to the local design based on the GSL. The reflection efficiencies obtained from local WAMs and estimated by the GSL are compared and analyzed for different reflection angles. Second, nonlocal interaction between the waterborne unit cells induced by the FSI is discussed through numerical simulation and theoretical analysis. Then, an optimization procedure based on diffraction theory is proposed to consider fully the nonlocal interaction between the waterborne unit cells. High-efficiency ultrathin WAMs for anomalous reflection at different angles are illustrated to confirm the presented strategy of nonlocal design. The underlying physical mechanism for high-efficiency reflections is also discussed. The validity of the scaling law with the FSI effect is later investigated for the WAM. Finally, we summarize the main findings of the present work.

II. LOCAL DESIGN BASED ON THE GSL

We first design a WAM by following the local design procedure of airborne acoustic metasurfaces [2,3], as illustrated in Fig. 1. According to the GSL, the relationship

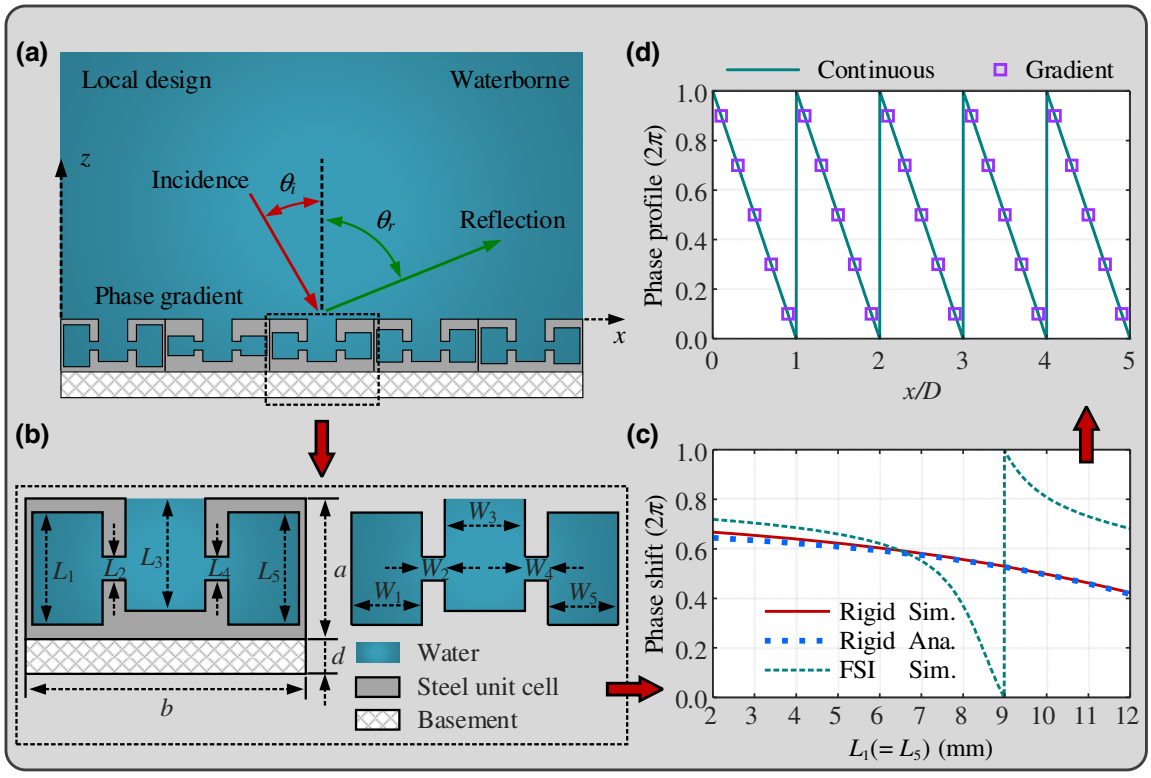

FIG. 1. Schematic of the local design for a WAM based on the GSL. (a) WAM based on the local design is composed of some discrete unit cells that provide local phase shifts. Based on the GSL, the incident waves can be reflected at an angle θ_r through the WAM with phase gradient on the basement. Panel (b) illustrates the cross section of the waterborne unit cell. The depth and width of the ith ($i = 1, \ldots, 5$) rectangular cavity are L_i and W_i, respectively. Panel (c) shows a full 2π range variation of the phase shift (green dashed lines) with the parameter $L_1(= L_5)$ for the unit cell with the FSI boundaries in (b), which is calculated by the finite-element model of a single unit cell with the periodic boundary condition. The analytical and simulated phase shifts for the unit cell with rigid walls are represented by blue dotted lines and red solid lines, respectively. Panel (d) shows the variation of the linear phase profile with coordinate x for anomalous reflection with $D = \lambda/|\sin\theta_i - \sin\theta_r|$, where the green solid line and purple squares represent the continuous and gradient phase profiles approximated by the local discrete unit cells, respectively.

between the incident and reflected waves in Fig. 1(a) can be expressed as

$$k(\sin\theta_i - \sin\theta_r) = d\Phi/dx, \tag{1}$$

where θ_i and θ_r represent the incident and reflection angles, respectively; $k = 2\pi f/c_w$ is the wave number in the water with the acoustic velocity $c_w = 1500\ \mathrm{ms}^{-1}$; f is the frequency; and $d\Phi/dx$ denotes the phase gradient along the x direction provided by discrete unit cells. Figure 1(b) shows the cross section of the unit cell used to construct the WAM. It consists of a straight channel with two Helmholtz resonators shunted in parallel, as well as a basement to mimic the practical case. The detailed geometrical parameters of the unit cell are listed in the Supplemental Material [32].

The phase shift of the reflected wave can be adjusted by tuning the geometrical parameter $L_1(=L_5)$. A finite-element model of a single unit cell with periodic boundary condition on its lateral boundaries is applied to predict the phase shift. Figure 1(c) shows the variation of the reflection phase shifts with $L_1(=L_5)$ for $f = 10$ kHz and $a = \lambda/10$ where $\lambda = c_w/f$. A full 2π coverage of the phase shift is obtained when the FSI boundaries are considered. In this way, we can approximate a continuous phase profile, e.g., for anomalous reflection illustrated in Fig. 1(d), by using local discrete unit cells with different geometrical parameters. Based on the local design of the WAM, the targeted anomalous reflection is expected to be achieved. Moreover, the phase shifts of the unit cell with rigid walls are also calculated by analytical and numerical methods, as shown in Fig. 1(c). The FSI is observed to have a great effect on the phase shifts of the unit cell, and should be considered in the design of the WAM. Detailed discussions can be found in Appendix A.

To test the feasibility of the local design, we take anomalous reflection at three different reflection angles as examples. Figures 2(a)–2(c) illustrate the cross sections of the designed periodic WAMs for $\theta_r = 36°$, $72°$, and $81°$ under normal incidence ($\theta_i = 0$). It is noted that periodic arrangement of unit cells is not necessary for the local design of a WAM based on the GSL. However, to compare with the following nonlocal design, we consider the periodic arrangement here. According to Eq. (1), the WAM should have a periodicity of $D = \lambda/\sin\theta_r$ for normal incidence ($\theta_i = 0°$). These values are approximately $D = 1.70\lambda$,

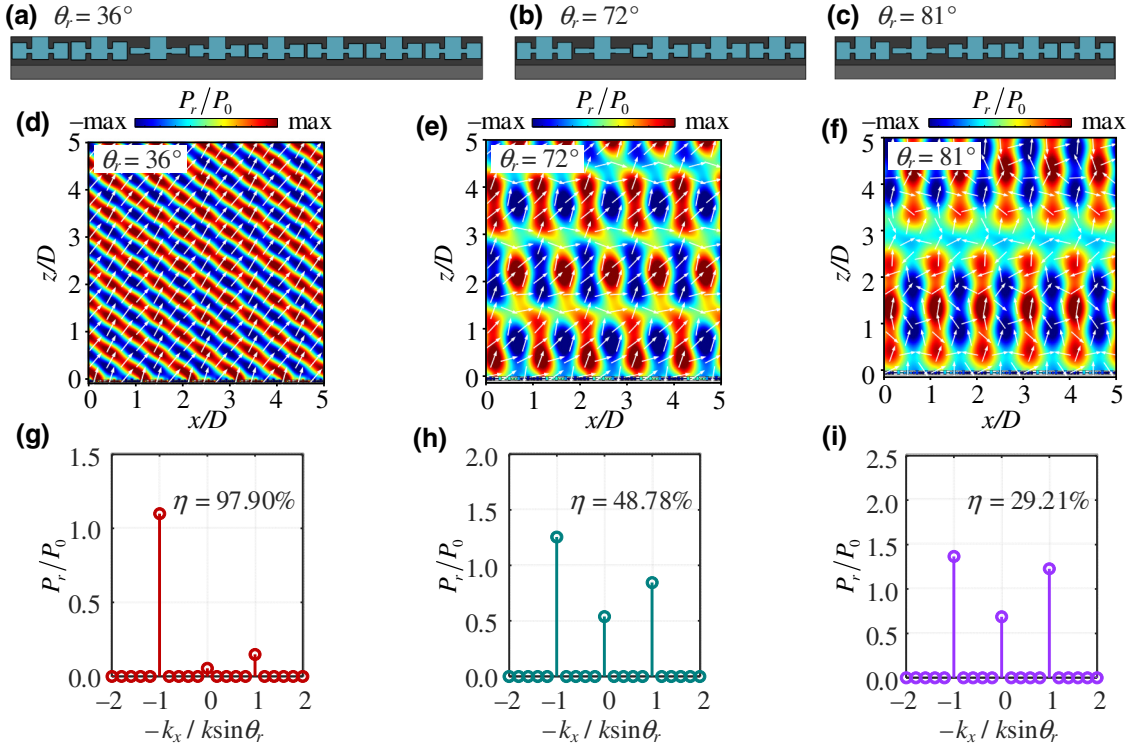

FIG. 2. Local design of the WAM for anomalous reflection. Panels (a)–(c) illustrate the cross sections of the WAMs based on the local design for $\theta_i = 0°$ and $\theta_r = 36°$, $72°$, and $81°$, respectively, the thickness of which is $\lambda/10$. The corresponding real parts of the reflected acoustic pressure fields are shown in (d) $\theta_r = 36°$, (e) $\theta_r = 72°$, and (f) $\theta_r = 81°$, where the white arrows indicate the local power intensity vector of the reflected acoustic pressure fields with $P_0 = 1$ Pa and max $= \sqrt{\cos\theta_i/\cos\theta_r}$ in the color bar; and perfectly matched layers with thickness $2D$ and typical wavelength 3λ are added at the top regions (not shown in figure) to eliminate the reflection at the boundaries. The corresponding FFT amplitudes of the reflected pressure on the transverse line located at $z = 2.5D$ as a function of $-k_x/k\ \sin\theta_r$ are presented for $\theta_r = 36°$ (g), $\theta_r = 72°$ (h), and $\theta_r = 81°$ (i), respectively.

1.05λ, and 1.01λ for the 36°, 72°, and 81° reflections, respectively. Furthermore, a unit cell having a $0-2\pi$ phase shift with slow variation is beneficial for local designs based on the GSL [33]. Such a condition may be satisfied when the width of the unit cell is about $\lambda/5$, as shown in Fig. 1(c). Therefore, the number of unit cells in a period is $M = \mathrm{INT}[D/(\lambda/5)]$ with INT[∗] representing a round-down operation, and there are eight, five, and five unit cells in a period for the 36°, 72°, and 81° reflections, respectively. Detailed geometrical parameters of the unit cells are listed in the Supplemental Material [32].

The simulated results of the reflected acoustic pressure fields for the three different angles are shown in Figs. 2(d)–2(f). The white arrows in the reflected fields represent the local power intensity vector, $\mathbf{I}_r = I_x\mathbf{e}_x + I_z\mathbf{e}_z$, where (I_x, I_z) can be calculated by $Re[p_r(\mathbf{v}_r)^*]/2$ with $\mathbf{v}_r = v_x\mathbf{e}_x + v_z\mathbf{e}_z = j\nabla p_r/(k\rho_w c_w)$ being the reflected velocity field ($\rho_w = 1000\ \mathrm{kgm}^{-3}$ is the density of the water), $\mathbf{e}_x$ and $\mathbf{e}_z$ are the unit vectors in the x and z directions, and "$_*$" represents the complex conjugate [16]. For the smallest reflection angle ($\theta_r = 36°$), the acoustic waves are basically redirected into the desired direction, although there are slight fluctuations in the reflection wavefronts. However, when the reflection angle is relatively big ($\theta_r = 72°$ and 81°), the reflection patterns become more chaotic. The directions of the arrows are diverse, suggesting the energy of the reflected waves flows in different directions.

Here, we use the reflection efficiency η to characterize quantitatively the performance of the local design [16,20]

$$\eta = \frac{\boldsymbol{\alpha}\cdot\mathbf{I}_r}{\boldsymbol{\alpha}\cdot\mathbf{I}_i} = \left(\frac{P_r}{P_0}\right)^2 \frac{\cos\theta_r}{\cos\theta_i} \times 100\%, \tag{2}$$

where $\boldsymbol{\alpha}$ is the normal vector of the WAM (here, $\boldsymbol{\alpha} = \mathbf{e}_z$); $\boldsymbol{\alpha}\cdot\mathbf{I}_i$ and $\boldsymbol{\alpha}\cdot\mathbf{I}_r$ represent the normal components of the power in the incident and desired reflection directions, respectively; and P_r/P_0 is the amplitude ratio of the incident and reflected waves in the desired direction (θ_r). Moreover, the theoretical values of P_r/P_0 for the GSL can be estimated by $2\cos\theta_r/(\cos\theta_i + c\cos\theta_r)$ [16], and the corresponding efficiencies are 98.89%, 72.14%, and 46.79% for the three angles. To determine P_r/P_0, we perform a fast Fourier transform (FFT) on the spatial position x [17,20,21]. Figures 2(g)–2(i) show the FFT amplitudes of the reflective acoustic pressure along a transverse line located at $z = 2.5D$ for the three angles, where $-k_x/k\ \sin\theta_r = -1$ represents the desired reflection direction, with the rest for other directions. Thus, the amplitudes of P_r/P_0 extracted at $-k_x/k\sin\theta_r = -1$ are 1.10, 1.26, and 1.37 for $\theta_r = 36°$, 72°, and 81°, respectively. The reflection efficiency η of the WAMs is then calculated by Eq. (2) to be 97.90%, 48.78%, and 29.21%. Obviously, the actual efficiency is close to the theoretical one at $\theta_r = 36°$, but significantly lower than the theoretical values at $\theta_r = 72°$ and 81°. However, the actual efficiency of an airborne acoustic metasurface can be accurately estimated even for large-angle reflections [16].

Unlike in airborne acoustic metasurfaces, the solid acts as an elastic body instead of a rigid one in WAMs because the FSI between the solid and water is more significant than that between the solid and air. To investigate the influence of the FSI, we follow the local design procedure to construct a series of WAMs for the aforementioned anomalous reflections. The channel-type unit cell is chosen to obtain the homogeneous phase shifts with and without FSI. The corresponding results are given in Appendix B. It is found that the reflection efficiencies for the rigid cases basically match the GSL theoretical prediction. In contrast, various deviations from the theoretical efficiency are observed in the cases with the FSI for different geometrical parameters, including the anomalous reflection for $\theta_r = 36°$. This means that the efficiency of the WAM for a specific reflection angle is no longer a constant that can be predicted by the GSL. It is highly dependent on the geometrical configurations when the FSI is involved. To further understand the significance of the FSI, we present a theoretical analysis for a simplified theoretical model with a coupled plate-fluid in Appendix C. The analysis intuitively shows that the FSI between water and solid is stronger than that between air and solid, and the vibration of the solid structure is highly dependent on its geometrical parameters for the water-solid case, which may result in different efficiencies for different combinations of unit cells in WAMs.

III. NONLOCAL INTERACTION BETWEEN THE WATERBORNE UNIT CELLS

The deviation between actual and theoretical efficiencies of the local WAMs is mainly attributed to the nonlocal interaction between the waterborne unit cells originating from the FSI. To demonstrate, we contrast the following three situations: a single unit cell, a homogeneous, and an inhomogeneous unit cell array (UCA). Figures 3(a)–3(c) show the corresponding reflected acoustic pressure fields and total displacements of the three systems at $f = 10$ kHz, where unit cells no. 1–5 are selected from the supercell in Fig. 2(b). In the calculation, the periodic boundary condition is imposed on the two sides of the waterborne area and single unit cell in Fig. 3(a). For the two UCAs in Figs. 3(b) and 3(c), the waterborne areas above the UCAs are separated by interior sound hard boundaries; the two sides of the waterborne areas are defined as the sound hard boundaries; and the two sides of the UCAs are set as the periodic boundaries. The uniform background pressure field serves as the incident wave and is exerted on the waterborne area over every unit cell in Figs. 3(a)–3(c). The FSI between water and solid is taken fully into account. A gradient phase shift for single unit cells no. 1–5 is observed in Fig. 3(a), satisfying the local design requirement. Meanwhile, the

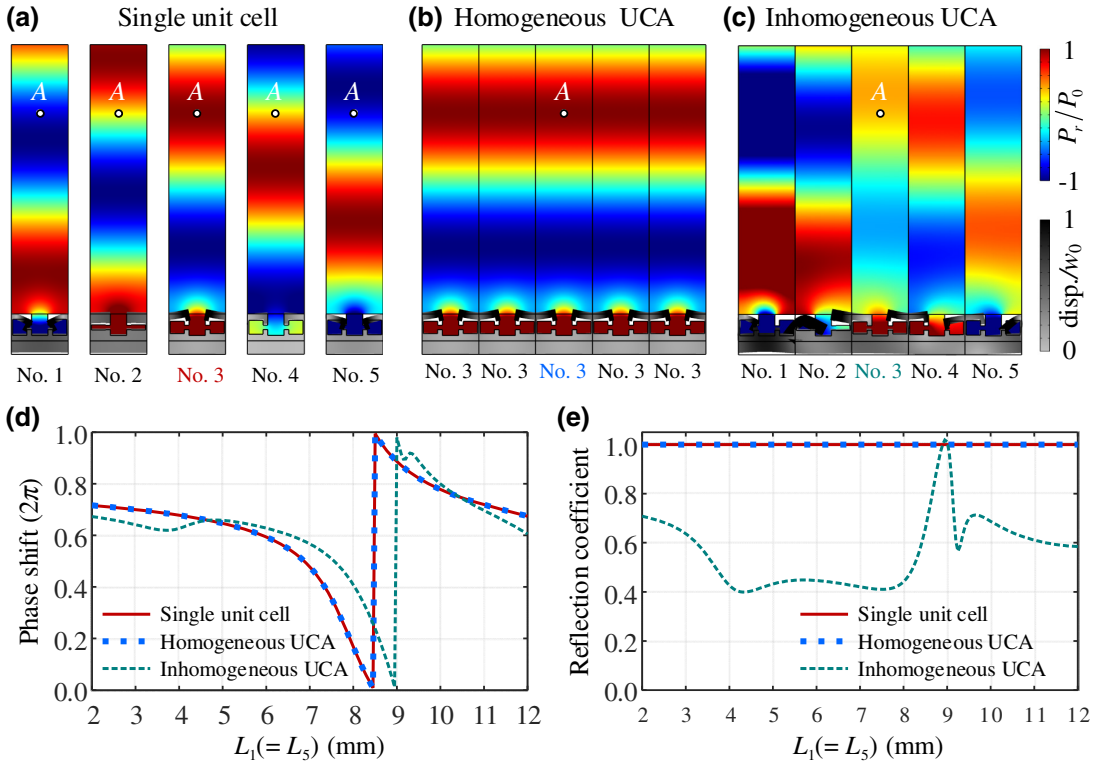

FIG. 3. Nonlocal interaction between the waterborne unit cells. Panels (a) to (c) show the real parts of the reflected acoustic pressure fields and total displacements for single unit cells no. 1–5, a homogeneous UCA of unit cell no. 3 and an inhomogeneous UCA of unit cells no. 1–5 at $f = 10$ kHz, respectively, where unit cells no. 1–5 in panels (a)–(c) are selected from five unit cells in Fig. 2(b); point A is an observation point 0.75λ away from the upper surface of the unit cell; and the phase shift and reflection coefficient are retrieved and normalized as $[\arg(P_r) + \pi]/2\pi$ and $|P_r|/P_0$, respectively, with $P_0 = 1$ Pa; $w_0 = 10^{-11}$ m; and the scale factor of the structural deformation is 2×10^8. Panels (d) and (e) show the phase shifts at point A and reflection coefficients varying with the parameter $L_1(= L_5)$ for the single unit cell in (a) (red solid lines), unit cell no. 3 in the homogeneous UCAs in (b) (blue dotted lines) and the inhomogeneous UCAs in (c) (green dashed lines).

reflected acoustic pressure field and the symmetrical structural deformation for single unit cell no. 3 in Fig. 3(a) are completely the same as those for the homogeneous UCA of unit cell no. 3 in Fig. 3(b). However, when different unit cells are assembled together, the acoustic pressure field in Fig. 3(c) is obviously changed for unit cell no. 3, and the asymmetrical structural deformation is observed. Since the waterborne areas above each unit cell in the UCA are strictly separated, these differences are mainly attributed to the change of the structural vibration for the inhomogeneous UCA induced by the FSI. As a result, the target gradient phase shift is distorted, and the acoustic pressure amplitude reflected by each unit cell in Fig. 3(c) is different from that reflected by the single unit cell in Fig. 3(a). However, these differences almost disappear among the airborne unit cells for the three cases. The detailed results are provided in Appendix D.

For quantitative analysis, we also extract the phase shift at point A and the normalized reflection coefficient of unit cell no. 3 in Figs. 3(a)–3(c) varying with geometrical parameter $L_1(= L_5)$. The results are plotted in Figs. 3(d) and 3(e), respectively. The phase shifts of a single unit cell and a homogeneous UCA perfectly coincide. However, a visible deviation can be found for the two UCAs in Figs. 3(b) and 3(c), and a phase difference of more than 93° appears at $L_1 = L_5 = 8.25$ mm. In addition, the reflection coefficients for the single unit cell and homogeneous UCA are both 1 for all values of L_1, while the result for unit cell no. 3 in the inhomogeneous UCA fluctuates between 0.399–1.019, and a peak value is obtained in the phase jumping region. Furthermore, the result for unit cell no. 3 in the inhomogeneous UCA in Fig. 3(c) may also change when it is integrated with different unit cells. This means that the practical boundary condition between the adjacent unit cells in the WAM can hardly be approximated by using the periodic boundary condition. The prearranged phase profile provided by each single unit cell may be disturbed when different unit cells are assembled. The nonlocal interaction between the waterborne unit cells makes it difficult to achieve target acoustic functions

by the local WAM based on the GSL. Furthermore, we discuss the influence of material parameters on the nonlocal interaction in Appendix E. The results show that the nonlocal interaction is universal for the WAMs with natural solid materials.

IV. NONLOCAL DESIGN BASED ON DIFFRACTION THEORY AND OPTIMIZATION

To overcome the restriction of the interaction between the waterborne unit cells, we adopt a nonlocal design concept by using diffraction theory and an optimization approach. Figure 4 shows the schematic of the nonlocal WAM for acoustic wave manipulation. The nonlocal WAM consists of periodic supercells. When an acoustic beam impinges on the WAM, as shown in Fig. 4(a), the reflected waves can be diffracted in different directions.

According to diffraction theory [20,22], the incident and reflected acoustic waves satisfy the following relationship

$$k(\sin\theta_i - \sin\theta_r) = NG_N, \tag{3}$$

where $G_N = 2\pi/D$, with D being the period length of a supercell, and $N = 0, \pm1, \cdots, \pm\infty \in Z$ representing the diffraction order. When $N = 1$ and $2\pi/D = d\Phi/dx$, Eq. (3) is reduced to the GSL in Eq. (1). Other values of N represent reflection waves in other directions. They are neglected and cannot be predicted by the GSL, resulting in poor efficiency of local design for large-angle reflections. The reflected acoustic pressure field $p_r(x,z)$ in Fig. 4(a) can be expressed as [20]

$$p_r(x,z) = \sum_N P_{r,N} exp[-j\,k_{xN}x - j\,k_{yN}z], \tag{4}$$

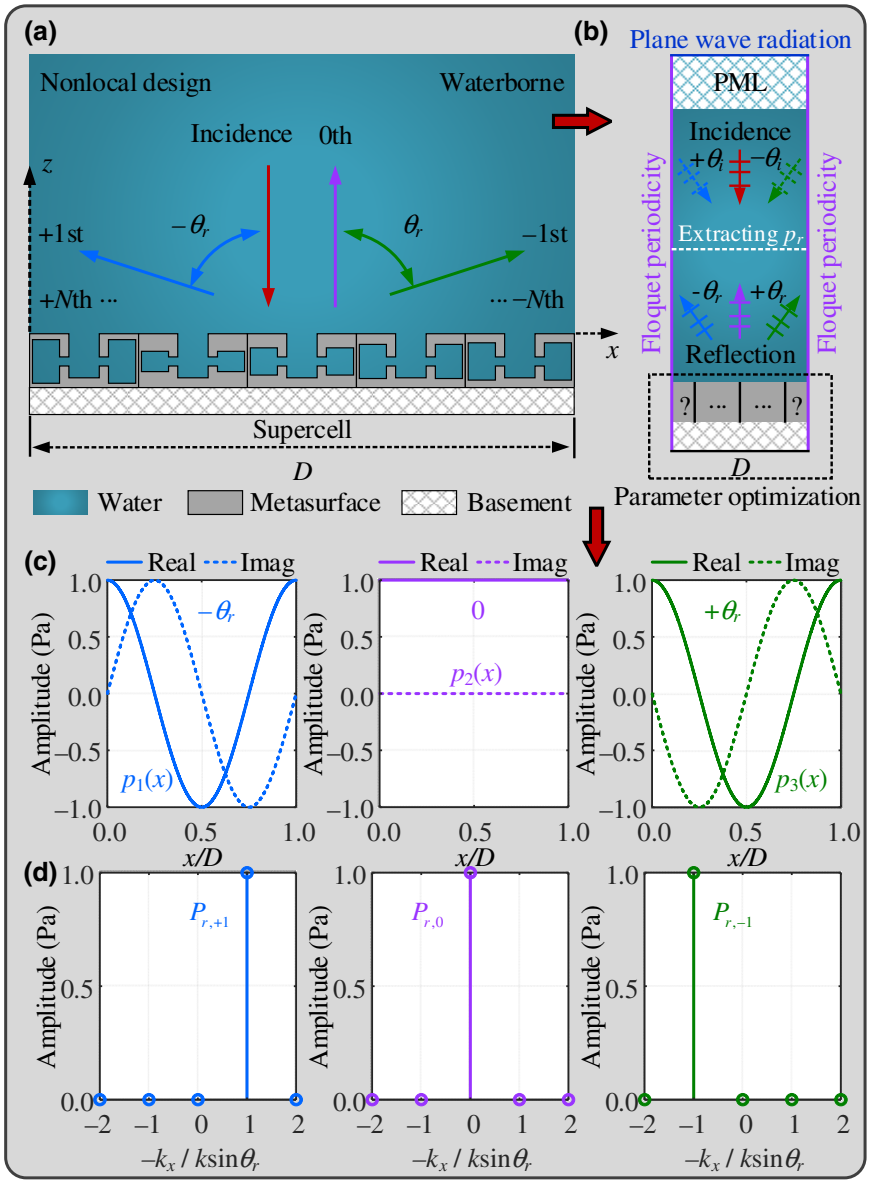

FIG. 4. Schematic of the nonlocal design for a WAM based on diffraction theory and optimization. (a) WAM based on the nonlocal design is composed of periodic supercells, where the period length of a supercell along the x direction is D. Based on diffraction theory, when an acoustic wave is incident from the negative z axis direction, there will be reflected waves of 0th, $\pm$1st,..., $\pm N$th order diffractive components above the WAM on the basement. Panel (b) illustrates the sketch of the nonlocal design combining diffraction theory and optimization. A background acoustic field at the specific incident angle $+\theta_i$, 0, or $-\theta_i$ serves as incident acoustic waves and is exerted on a supercell with Floquet periodicity. Reflection acoustic pressure on the transverse line is extracted to analyze the reflected waves in different directions ($+\theta_r$, 0, or $-\theta_r$, etc.) with FFT. Driven by the objective function of reflection efficiency, a parameter optimization procedure with genetic algorithm is applied to reverse design the WAM. Panel (c) shows the variation of the real and imaginary parts of the acoustic pressure with x/D for $p_1(x) = exp(ik\sin\theta_r x)$ (1st column), $p_2(x) = 1$ (2nd column), and $p_3(x) = exp(-ik\sin\theta_r x)$ (3rd column). The corresponding FFT amplitudes of the above acoustic pressure are presented in (d).

where $P_{r,N}$ denotes the amplitude of the reflected acoustic wave at $\theta_{r,N}$; $k_{xN} = k\sin\theta_{r,N} = k\sin\theta_i - NG_N$; and $k_{yN} = \sqrt{k^2 - (k\sin\theta_i - NG_N)^2}$. The real k_{yN} is yielded only when $k^2 > (k\sin\theta_i - NG_N)^2$. Hence, the infinite summation in Eq. (4) only contains finite propagating modes.

Figure 4(b) illustrates the sketch for the nonlocal design. Several unit cells are integrated in the supercell with a period of D. The determination of D is essential for the design of the WAM. Take anomalous reflection as an example; Eq. (3) is simplified as $-k\sin\theta_r = NG_N$ for normal incidence ($\theta_i = 0$). We can select $D = \lambda/|\sin\theta_r|$. Then the desired reflection direction θ_r corresponds to $N = -k_x/k\sin\theta_r = -1$. For oblique incidence ($\theta_i \neq 0$), we select $D = [D_i, D_r]$ with $D_i = \lambda/|\sin\theta_i|$ and $D_r = \lambda/|\sin\theta_r|$ being the periods of incident and reflected waves, respectively, and $[*,*]$ denoting the operation of least common multiple. Since the periodicity of the incident and reflected waves is considered, the reflection direction can be determined by $-k\sin\theta_r = NG_N$. In particular, $D = \lambda/|\sin\theta_r|$ for $\theta_i = -\theta_r$. Similarly, $N = -k_x/k\sin\theta_r = -1$ yields the desired reflection direction θ_r. Next, we use numerical methods to retrieve the reflected amplitudes in different directions. In Fig. 4(b), a background acoustic field at specific incident angle $+\theta_i$, 0 or $-\theta_i$ serves as the incident acoustic field and is exerted above the supercell. A perfectly matched layer (PML) with thickness $2D$ and typical wavelength 3λ is added on the top. Plane wave radiation is imposed on top of the PML to further eliminate reflections. Floquet periodicity is applied to the sides of the supercell. Reflected acoustic pressure along a transverse line is extracted to analyze the reflected waves in different directions ($+\theta_r$, 0, $-\theta_r$, etc.) with FFT. Figure 4(c) shows the variation of the real and imaginary parts of three special acoustic waves $p_1(x) = exp(ik\sin\theta_r x)$, $p_2(x) = 1$ and $p_3(x) = exp(-ik\sin\theta_r x)$, corresponding to the reflected waves at angles of $-\theta_r$ (1st column), 0 (2nd column), and θ_r (3rd column), respectively. The corresponding FFT amplitudes are shown in Fig. 4(d). Peak values of 1 appear at $-k_x/k\sin\theta_r = 1$, 0, and -1, respectively. By this means, the reflection amplitudes in different directions can be accurately recognized.

Next, we employ an optimization procedure to reverse design the WAM. The basic unit cell selected is that in Fig. 1(b). The geometrical parameters L_i and $W_i (i = 1, \cdots, 5)$ in each unit cell are simultaneously optimized to obtain a unitary reflection efficiency. Meanwhile, some geometrical constraints are introduced to ensure the connectivity and compatibility of the optimized unit cells. For nonlocal WAM with high-efficiency anomalous reflection, the optimization with multiple constraints is formulated as

$$\begin{aligned}\text{Find: } &\mathbf{L}_m = [L_{m,1}, \cdots, L_{m,5}],\\ &\mathbf{W}_m = [W_{m,1}, \cdots, W_{m,5}], m = 1, \cdots, M;\end{aligned} \tag{5-1}$$

$$\text{Minimizing: fitness} = \sum_{N_{UW}} |P_{r,N_{UW}}/P_{r,N_W}|^2, N_{UW}, N_W \in Z, N_{UW} \neq N_W; \tag{5-2}$$

$$\text{Subject to: } \begin{cases} e \le L_{m,j} \le a - 2e, e = a/20, j = 1,2,4,5,\\ a/2 + e \le L_{m,j} \le a - e, j = 3,\\ \sum_{j=1}^{5} W_{m,j} = b - 2e,\\ e \le W_{m,j} \le \varepsilon(b - 2e), j = 1, \cdots, 5, \end{cases} \tag{5-3}$$

where $\mathbf{L}_m$ and $\mathbf{W}_m$ are the geometrical parameters of the cavities for the mth unit cell in a supercell with M unit cells; $P_{r,N_{UW}}$ and P_{r,N_W} are the reflection amplitudes in unwanted and wanted directions with N_{UW} and N_W being their corresponding diffraction order. For anomalous reflection at $+\theta_r$, $N_W = -k_x/k\sin\theta_r = -1$ with N_{UW} taking the integers other than N_W. In terms of geometrical constraints in Eq. (5-3), a is the thickness of the supercell; e is the minimal size constraint; $b = D/M$ is the width of the unit cell; $L_j (j = 1,2,4,5)$ and $L_j (j = 3)$ in each unit cell are limited to $(e, a - 2e)$ and $(a/2 + e, a - e)$, respectively, to ensure the connectivity of each unit cell when their sizes change; the limit for the sum of W_j in each unit cell is $b - 2e$ to ensure all cavities are compatible; W_j is limited to $(e, \varepsilon b - 2\varepsilon e)$ with $\varepsilon = 4/5$ in order to provide a sufficient variation range; and a ratio limit of $W_1 : W_2 : W_3 : W_4 : W_5 = 3 : 1 : 4 : 1 : 1$ obtained by optimization tests is added when the sum constraint of W_j is not satisfied. To solve the inverse design problem described by Eq. (5), we use COMSOL Livelink with MATLAB to calculate the reflected acoustic pressure field of the WAM, and a genetic algorithm with continuous variables is used to perform the optimization procedure for the WAM with high-efficiency anomalous reflection. The maximum reflection efficiency is obtained when the minimum fitness is reached. And the nonlocal design can fully consider the nonlocal interaction between the waterborne unit cells caused by the FSI effect.

V. HIGH-EFFICIENCY ULTRATHIN WAM

To demonstrate, we begin with the previously mentioned three cases for anomalous reflection ($\theta_i = 0°$, $\theta_r = 36°$, $72°$, and $81°$) to validate the practicability of the nonlocal design. In the optimization, the thickness of the supercell and basement are selected as $a = \lambda/10$ and $d = \lambda/20$, respectively. For comparison, we take the same numbers of unit cells in a supercell as in the local WAMs, i.e., eight for the $36°$ reflection, and five for $72°$ and $81°$ reflections. $N_W = -1$ with $N_{UW} = -2$, 0, $+1$, $+2$ is considered in the fitness function. Figures 5(a)–5(c) illustrate the cross sections of the optimal WAMs in a period based on the nonlocal design for $\theta_r = 36°$, $72°$, and $81°$ under normal incidence ($\theta_i = 0$), respectively. It can be observed

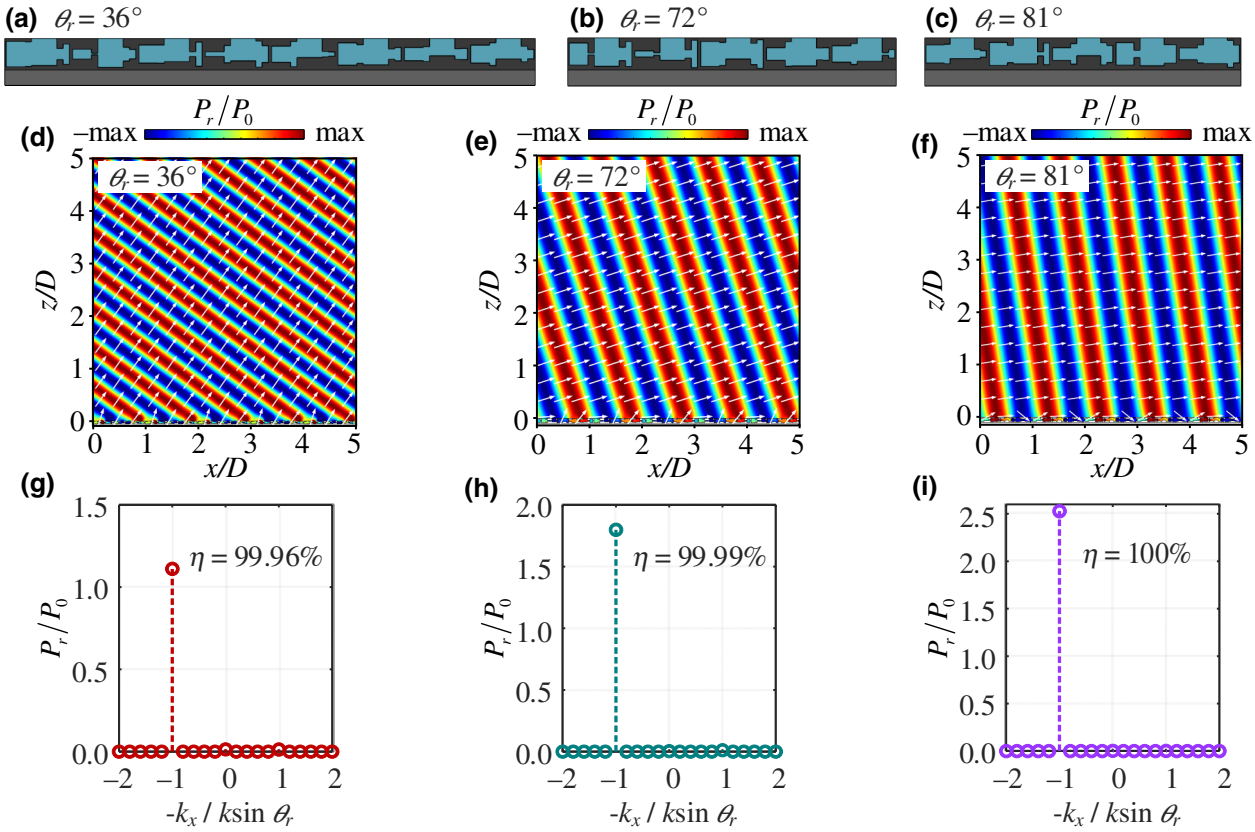

FIG. 5. Nonlocal design of the WAM for anomalous reflection. Panels (a)–(c) illustrate the cross sections of the WAMs based on the nonlocal design for $\theta_i = 0°$ and $\theta_r = 36°$, 72°, and 81°, respectively, the thickness of which is $\lambda/10$. The corresponding real parts of the reflected acoustic pressure fields are shown in (d) $\theta_r = 36°$, (e) $\theta_r = 72°$, and (f) $\theta_r = 81°$, where the white arrows indicate the local power intensity vector of the reflected acoustic pressure fields with $P_0 = 1$ Pa and max $= \sqrt{\cos\theta_i/\cos\theta_r}$ in the color bar; and perfectly matched layers with thickness $2D$ and typical wavelength 3λ are added at the top regions (not shown in figure) to eliminate the reflection at the boundaries. The corresponding FFT amplitudes of the reflected pressure on the transverse line located at $z = 2.5D$ as a function of $-k_x/k \sin\theta_r$ are presented for $\theta_r = 36°$(g), $\theta_r = 72°$ (h), and $\theta_r = 81°$ (i), respectively.

that many irregular and asymmetrical unit cells appear in the supercell. Detailed geometrical parameters of the unit cells are listed in the Supplemental Material [32].

Full-wave simulations are then performed to verify our design. The real parts of the simulated acoustic pressure fields of the nonlocal WAMs are presented in Figs. 5(d)–5(f) for the three different angles. It is obvious that the optimal nonlocal WAMs exhibit uniform and ordered reflected pressure fields for the three reflection angles. The white arrows in the reflected fields represent the local power intensity vector. These arrows above the WAMs all point in the direction of the reflection angle, implying that all the incident power flows in the desired reflection direction. Furthermore, the FFT amplitudes of the reflected fields along a transverse line located at $z = 2.5D$ varying with $-k_x/k \sin\theta_r$ are shown in Figs. 5(g)–5(i) for $\theta_r = 36°$, 72°, and 81°, respectively. It is observed that the optimal nonlocal WAMs can greatly suppress the reflected waves in unwanted directions and present a peak value only in the target direction ($N = -k_x/k \sin\theta_r = -1$). The FFT amplitudes at ($-k_x/k \sin\theta_r = -1$) with the nonlocal WAMs are 1.1116, 1.7988, and 2.5287, respectively, and these are extremely close to the theoretical values of 1.1118, 1.7989, and 2.5283 calculated from $\sqrt{\cos\theta_i}/\sqrt{\cos\theta_r}$. This indicates that almost 100% of the incident energy is reflected in the desired direction. The reflection efficiencies break the theoretical upper limits of 98.89%, 72.14%, and 46.79% from the GSL prediction, and they are about 2.06%, 51.21%, and 70.79% higher than those of the local designs for $\theta_r = 36°$, 72°, and 81°, respectively [see Figs. 2(g)–2(i)]. This high-efficiency wave manipulation results from the nonlocal design. It should be noted that the peak value may be slightly larger than the theoretical value due to the error brought by the FFT.

In addition, the thickness of the WAM can be further decreased to $\lambda/30$ or even $\lambda/60$. As an example, the high-efficiency anomalous reflection for the oblique incidence of $\theta_i = -72°$ with $\theta_r = 72°$ is implemented with a similar optimization procedure. The thickness of the supercell a is

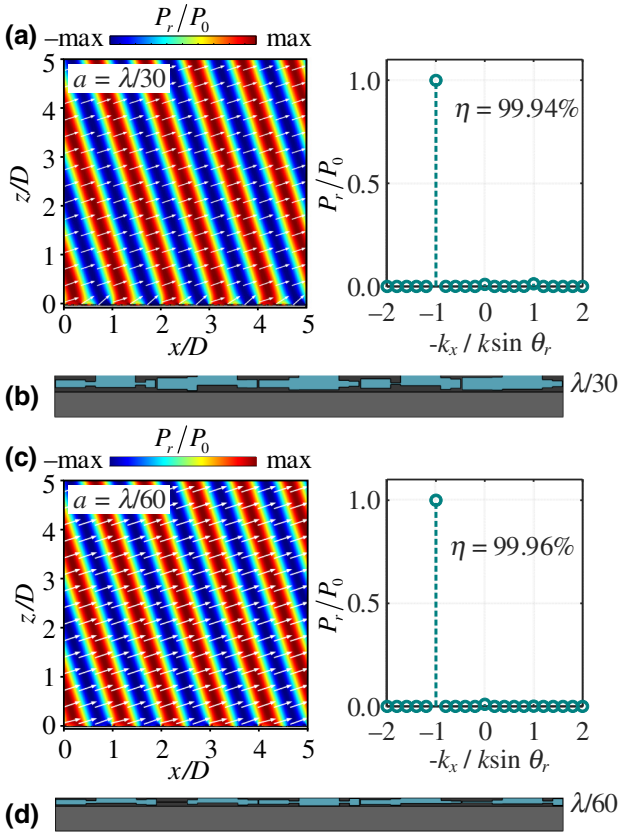

FIG. 6. High-efficiency ultrathin WAM for anomalous reflection under oblique incidence. Real parts of the reflected acoustic pressure fields (1st column) and the corresponding FFT amplitudes (2nd column) of the reflected pressure on a transverse line located at $z = 2.5D$ are presented for two ultrathin WAMs with thicknesses of $\lambda/30$ (a) and $\lambda/60$ (c), respectively, where $P_0 = 1$ Pa and max $= \sqrt{\cos\theta_r/\cos\theta_i}$ with $\theta_i = -72^\circ$ and $\theta_r = 72^\circ$ in the color bar; and perfectly matched layers with thickness $2D$ and typical wavelength 3λ are added at the top regions (not shown in figure) to eliminate the reflection at the boundaries. Panels (b) and (d) illustrate the cross sections of the WAMs with thicknesses of $\lambda/30$ and $\lambda/60$, respectively.

reduced to $\lambda/30$ and $\lambda/60$, respectively; the thickness of the basement d remains unchanged at $\lambda/20$; and $N_W = -1$ with $N_{UW} = -2,\ 0,\ +1,\ +2$ is considered in the fitness function. The reflected acoustic pressure fields and the corresponding FFT amplitudes of the two ultrathin WAMs are presented in Figs. 6(a) and 6(c), respectively. The cross sections of the optimal WAM with five unit cells in a period are illustrated in Figs. 6(b) and 6(d). Detailed geometrical parameters are listed in the Supplemental Material [32]. It can be seen that nearly all the energy is reflected in the desired direction. The reflection efficiencies reach over 99.94% ($a = \lambda/30$) and 99.96% ($a = \lambda/60$), respectively. This implies that the nonlocal interaction between the waterborne unit cells induced by the FSI is beneficial to high-efficiency acoustic wave manipulation with an ultrathin structure.

Actually, the underlying physical mechanism for the present high-efficiency WAMs is consistent with the impedance-matched theory [16], although the high-efficiency reflections are obtained through numerical optimization with diffraction theory rather than analytically. This suggests that the transverse energy channeling along the designed WAM can be satisfied by optimizing a nonlocal supercell. Next, we present the detailed analysis.

In terms of the anomalous reflection, the normal components of the incident, reflected, and total intensity vectors along the metasurface can be calculated by [16,18]

$$I_{\text{inc}}(x,0) = \mathbf{e}_z \cdot \mathbf{I}_i = -\frac{1}{2}\frac{P_0^2\cos\theta_i}{Z_w}, \tag{6-1}$$

$$I_{\text{re}}(x,0) = \mathbf{e}_z \cdot \mathbf{I}_r = \frac{1}{2}\frac{A^2P_0^2\cos\theta_r}{Z_w}, \tag{6-2}$$

$$I_{\text{tot}}(x,0) = \mathbf{e}_z \cdot \mathbf{I}_t = \frac{P_0^2}{2Z_w}\left[(A^2\cos\theta_r - \cos\theta_i) + A\cos\Phi(x)(\cos\theta_r - \cos\theta_i)\right], \tag{6-3}$$

where $Z_w = \rho_w c_w$ and $A = P_r/P_0$. For the unitary reflection, the energy conservation law ($|I_{\text{inc}}| = |I_{\text{re}}|$) requires $A = \sqrt{\cos\theta_i/\cos\theta_r}$. Thus, the theoretical impedance on the WAM for high-efficiency anomalous reflection can then be expressed as [16,18]

$$Z_s = \frac{p_t(x,0)}{-[0,\mathbf{e}_z]\cdot v_t(x,0)} = Z_w\frac{\sqrt{\cos\theta_r} + \sqrt{\cos\theta_i}e^{-i\Phi(x)}}{\cos\theta_i\sqrt{\cos\theta_r} - \sqrt{\cos\theta_i}\cos\theta_r e^{-i\Phi(x)}}, \tag{7}$$

where $\Phi(x) = k(\sin\theta_i - \sin\theta_r)x$.

Take anomalous reflection of $\theta_r = 72^\circ$ with $\theta_i = 0^\circ$ as an example. Figure 7(a) presents the theoretical impedance distribution calculated by Eq. (7) at $f = 10$ kHz. It is observed that the required impedance is necessarily active [$\text{Re}(Z_s) < 0$] or lossy [$\text{Re}(Z_s) > 0$] for the unitary reflection. However, due to the nonlocal interaction between the waterborne unit cells, we can hardly obtain the exact impedance of a single unit cell in an inhomogeneous UCA. Thus, such a condition is difficult to satisfy directly by discretizing the impedance profiles with isolated unit cells. However, it can be implicitly realized by optimizing a periodic supercell with nonlocal interactions based on diffraction theory. By setting the reflection efficiency as the target, the optimal supercell could be found through the optimization procedure to achieve a high-efficiency reflection. Then the impedance mismatch between the incident and reflected waves will be naturally resolved when the optimal reflections are obtained.

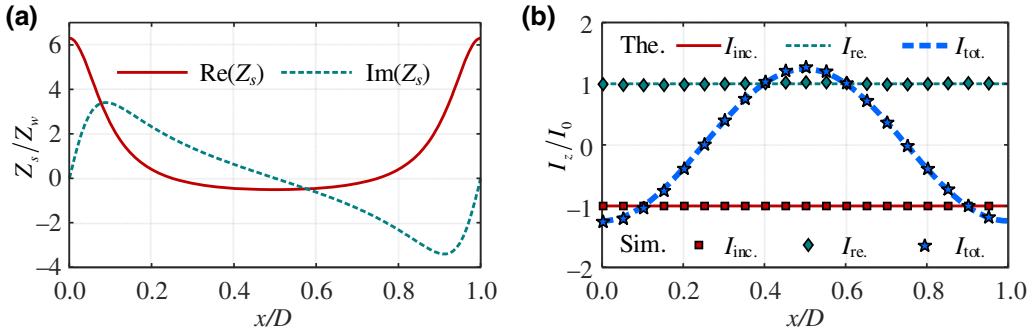

FIG. 7. Impedance and intensity distribution on the WAM. Panel (a) shows the impedance profiles of the WAM with the unitary reflection efficiency for $\theta_r = 72°$ with $\theta_i = 0°$. Panel (b) shows the corresponding normal components of the incident, reflected, and total intensity vectors as functions of coordinate x, where $D = \lambda/|\sin\theta_i - \sin\theta_r|$ and $I_0 = P_0^2/(2Z_w)$. The theoretical results are obtained from Eq. (6), and simulated ones are retrieved from the transverse line located at $z = 0.5D$ within $0.1375D \le x \le 1.1375D$ in Fig. 5(e).

To illustrate, the normal intensity components I_{inc}, I_{re}, and I_{tot} at $z = 0$ obtained from Eq. (6) are shown in Fig. 7(b). Since the energy intensity is periodic with coordinate x, the energy distribution in any period has an identical profile. It is clear that I_{tot} is negative for $\mathrm{Re}(Z_s) > 0$ and positive for $\mathrm{Re}(Z_s) < 0$, but its average value is zero within a period. Thus, the required energy distribution can be realized by a passive lossless nonlocal design [18]. To verify this, we plot the simulated energy intensity for the designed WAM in Fig. 7(b) by using scattered symbols. To avoid the influence of the near-field scattering, the results are taken from the transverse line at $z = 0.5D$ for the 72° reflection in Fig. 5(e). The simulated results in a period ($0.1375D \le x \le 1.1375D$) agree very well with the theoretical ones. This implies that the energy can be transferred between the adjacent unit cells and redistributed through the nonlocal interaction. Therefore, the theoretical energy distribution is well satisfied through the optimization of a supercell.

It is noted that the numerical results may be more accurate with a finer mesh, but this will cost more in computing resources. In our calculation, the size of the narrowest region is $e = a/20$. To illustrate the practicability of the ultrathin design, the maximum element size limitations are set as $a/60$ and $\lambda/50$ for the supercell layer and the rest, respectively. It is found that the efficiency of the optimal WAM has almost no decrease for a WAM with the thickness of $\lambda/30$ when the thermoviscous effect is considered. With the decrease in the thickness, the thermoviscous effect becomes more pronounced. A relatively high efficiency could be maintained when the thermoviscous effect is included in the optimization procedure. Detailed analysis is provided in the Supplemental Material [32].

VI. UNIVERSAL SCALING LAW WITH THE FSI

A scaling law holds for the WAM consisting of a layered homogeneous medium [34]. In this part, we investigate the universality of the scaling law for a WAM with the FSI. Taking the optimal metasurface in Fig. 5(e) as an example, we change the operating frequency f from 1 to 100 kHz. The geometrical parameters of the WAM are

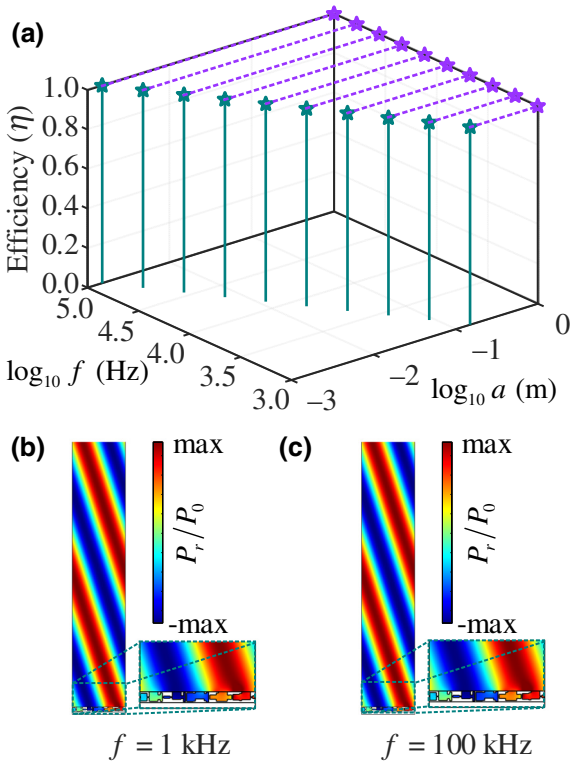

FIG. 8. Scaling law between the unit cell size and operating wavelength. Panel (a) shows the variation of the reflection efficiency η of the scaled WAM in Fig. 5(e) with operating frequency $\log_{10} f$ and $\log_{10} a$. Panels (b) and (c) present the real parts of the reflected acoustic pressure fields within one supercell ($0 \le x \le D$ and $z \le 5D$) when $f = 1$ kHz and $f = 100$ kHz, respectively, where D is the corresponding width of a supercell; $P_0 = 1$ Pa; and $\max = \sqrt{\cos\theta_r/\cos\theta_i}$ with $\theta_i = 0°$ and $\theta_r = 72°$ in the color bar.

simultaneously scaled in proportion to the working wavelength. The reflection efficiency of the scaled metasurfaces calculated by Eq. (2) is shown in Fig. 8(a). The scaled metasurfaces maintain nearly 100% reflection efficiency in the considered frequency range. The reflected pressure fields for $f = 1$ kHz and $f = 100$ kHz are quite uniform, as shown in Figs. 8(b)–8(c). Thus, the FSI effect between the water and structure is universal over a very wide frequency range, and the scaling law is valid between the unit cell size and the operating wavelength.

VII. CONCLUSIONS

In summary, a nonlocal design strategy combining diffraction theory and an optimization method is proposed to design a high-efficiency ultrathin WAM. As a comparison, a local design based on the GSL is also implemented. Results show that the FSI between water and solid enhances the nonlocal interaction between the waterborne unit cells. The phase shifts provided by inhomogeneous unit cells assembled together can hardly be predicted by a single unit cell with the periodic boundary condition. The local design cannot guarantee the expected acoustic function. However, the proposed design strategy can fully consider the nonlocal interaction between unit cells induced by the FSI, thus breaking the inherent efficiency limitation of the GSL. High-efficiency anomalous reflections are successively performed using ultrathin WAMs to confirm the practicability of the nonlocal design concept. The thickness of the WAM with unitary efficiency can be reduced to one tenth or even one sixtieth of the working wavelength. The required energy distribution for the high-efficiency design based on the impedance-matched theory is naturally satisfied through the optimization of the nonlocal supercell. In addition, the scaling law for the WAM with the FSI is proved to be valid over a wide frequency range. Such ultrathin and high-efficiency design is expected to further promote practical applications of metasurfaces in lightweight and high-performance waterborne acoustic devices.

Finally, we would like to mention that the main goal of the present research is to examine the influence of the FSI and propose a nonlocal design strategy for a high-efficiency WAM based on diffraction theory and an optimization method. The geometrical parameters used in this paper are just chosen for verification. For actual experiment and production, actual size and accuracy should be considered in the optimization to make the fabrication easier and more convenient. This can be done by setting necessary constraint conditions into the optimization model.

ACKNOWLEDGMENTS

This work is supported by National Natural Science Foundation of China (Grants No. 11972246, No. 11991032, No. 12072223, No. 11991031, and No. 12021002).

APPENDIX A: INFLUENCE OF FSI ON THE PHASE SHIFT OF A UNIT CELL

When the walls of the unit cell are regarded as rigid, we can adopt the lumped-parameter model to calculate the acoustic impedance of the unit cell. Figure 9(a) shows the schematic diagram of the unit cell with rigid walls. It is composed of a straight channel with two Helmholtz resonators shunted in parallel. According to the electroacoustic analogy method [35,36], the upper part of the straight channel can be equivalent to an acoustic mass M_{31}, and the lower part is regarded as a closed tube, which is treated as an acoustic compliance C_{32} plus an acoustic mass M_{32}. For the two Helmholtz resonators, the neck and cavity are equivalent to an acoustic mass $M_2(M_4)$ and an acoustic compliance $C_1(C_5)$, respectively. The effective circuit model of the unit cell is illustrated in Fig. 9(b). Thus, the total acoustic impedance of the unit cell with the rigid walls can be expressed as

$$Z_s = Z_{M_{31}} + \frac{1}{1/(Z_{M_2} + Z_{C_1}) + 1/(Z_{C_{32}} + Z_{M_{32}}) + 1/(Z_{M_4} + Z_{C_5})} \tag{A1}$$

where the impedances of the acoustic mass and acoustic compliance can be expressed as [35]

$$\begin{aligned} Z_{M_{31}} &= j\omega\rho_w L_{31}/W_3,\ Z_{M_2} = j\omega\rho_w(W_2 + \Delta W_2)/L_2, \\ Z_{M_{32}} &= j\omega\rho_w L_{32}/(3W_3),\ Z_{M_4} = j\omega\rho_w(W_4 + \Delta W_4)/L_4, \\ Z_{C_1} &= -j\rho_w c_w^2/(\omega L_1 W_1),\ Z_{C_{32}} = -j\rho_w c_w^2/(\omega L_{32} W_3), \\ Z_{C_5} &= -j\rho_w c_w^2/(\omega L_5 W_5), \end{aligned}$$

with $L_{31} = a/2$; $L_{32} = L_3 - L_{31}$; ΔW_2 and ΔW_4 being the corrections of the lengths induced by the added acoustic masses due to radiation for the Helmholtz resonators [35];

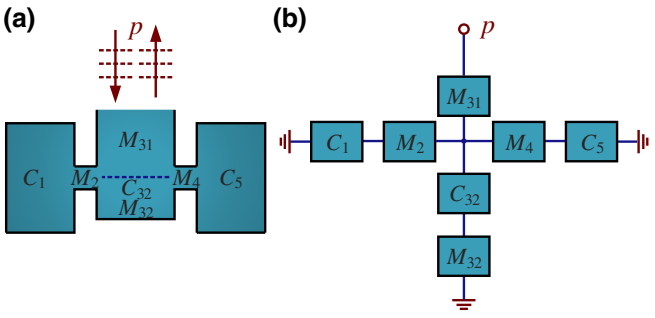

FIG. 9. Theoretical effective model of the unit cell. Panel (a) shows the schematic diagram of the unit cell with rigid walls. Panel (b) illustrates the effective circuit model of the unit cell with rigid walls to derive the phase shift.

and $\omega = 2\pi f$ being the angular frequency. Based on the acoustic impedance of the unit cell, the reflection coefficient r of the unit cell can be approximately expressed as [36]

$$r = (Z_s - Z_w/b)/(Z_s + Z_w/b), \tag{A2}$$

The analytical phase shift can then be retrieved and normalized by

$$\phi_{\text{ana}} = \{\arctan[\text{Im}(r)/Re(r)] + \pi\}/(2\pi) + \phi_0. \tag{A3}$$

where ϕ_0 is the phase correction constant. Here, considering the symmetry in the unit cell, we select $\Delta W_2 = \Delta W_4 = 1.7L_2$ and $\phi_0 = 0.18$ as the corrections. Figure 1(c) shows the analytical and simulated phase shifts of the unit cell varying with the parameter $L_1(= L_5)$. The analytical formula can perfectly predict the varying trend of the phase shift with a slight deviation for relatively small values of $L_1(= L_5)$ since the Helmholtz resonator is close to a tube in such cases. However, this analytical model only works well for the rigid wall assumption. When FSI is considered on the boundaries between the water and solid, an apparent deviation in phase shift can be observed compared to that for the rigid walls, see Fig. 1(c). Thus, the FSI has a distinct influence on the phase shift and should be taken into account in the design of WAMs.

APPENDIX B: INFLUENCE OF FSI ON THE LOCAL WAM

Based on the GSL, the phase shifts of a single unit cell varying with geometrical parameters should be first established before designing metasurfaces. For airborne acoustic metasurfaces, periodic boundaries are generally applied to a single unit cell to retrieve the phase shift in COMSOL Multiphysics. Similarly, we perform the same procedure to design the local WAM. Due to the high impedance contrast between water and air, the FSI between water and solid cannot be neglected. We build the channel-type unit cell models with rigid and FSI boundaries, illustrated in Fig. 10(a). The thickness and width of the unit cell on the basement with thickness $d = \lambda/20$ are a and b, respectively. The depth and width of the channel are L and $W = b - 2e$ with $e = \lambda/50$. For the rigid case, the solid structures are neglected, and the solid boundaries are regarded as sound hard walls. For the case with FSI, the solid structures are defined as linear elastic materials, and the acoustic structure coupling boundaries are fully considered. In addition, the periodic boundary condition is also applied to the two cases. Figure 10(a) shows the simulated phase shifts of the single unit cell with rigid and FSI boundaries at $f = 10$ kHz, where $a = \lambda/2 + e$ and $b = \lambda/(8 \sin\theta_r)$ with $\theta_r = 36^\circ$. It is observed that the phase curves of both basically coincide. The FSI has a slight influence on the phase shifts of the single channel-type unit cell with the periodic boundary condition.

Next, we assemble discrete unit cells together to make up the WAMs. According to the GSL, the phase distribution of anomalous reflection is $k(\sin\theta_i - \sin\theta_r)x + C$, where k is the wave number in the water; θ_i and θ_r represent the incident and reflected angles; x is the position coordinate; and C is an arbitrary phase constant. We can select different phase constants C to construct a series of local WAMs with the same phase gradient but different geometrical structure. This may bring various FSIs between water and WAMs due to the abundant geometric configurations. Three different reflection angles ($\theta_r = 36^\circ$, 72°, and 81°) for normal incidence ($\theta_i = 0^\circ$) are considered. It is noted that the width b of the unit cell is recalculated by $b = \lambda/(M \sin\theta_r)$ from each θ_r, where $M = 8$, 5, and 5 for $\theta_r = 36^\circ$, 72°, and 81°, respectively, and the phase shifts of the unit cell are also recalculated according to the corresponding geometrical parameters. The reflection efficiency η calculated by Eq. (2) is used to quantitatively analyze the influence of the FSI. Figure 10(b) shows the variation of the reflection efficiency (η) of the local WAM with rigid and FSI boundaries as a function of θ_r. Meanwhile, the theoretical efficiency of the GSL is also plotted in Fig. 10(b). A total of 12 phase constants C varying from $\pi/6$ to 2π with a step of $\pi/6$ are selected to design the local WAMs. Detailed geometrical parameters are list in the Supplemental Material [32]. For the rigid cases of different reflected angles, the reflection efficiency η fluctuates in a small range for different phase constants C, and meets the GSL theoretical prediction. In contrast, a larger fluctuation in the efficiency η can be observed in the case with FSI boundaries. The efficiency η changes more dramatically with C for larger reflected angles and deviates noticeably from the theoretical expectation of the GSL. It depends closely on the geometrical shape of the metasurface. For a clear demonstration, the FFT amplitudes and the acoustic pressure fields within a supercell with rigid and FSI boundaries for $C = 2\pi$ are shown in Figs. 10(c)–10(d). When $-k_x/k \sin\theta_r = -1$, the acoustic waves are reflected at the expected angle θ_r. Other values of $-k_x/k \sin\theta_r$ represent other reflection directions. Compared with the rigid cases, it can be found that the FSI effect can enhance or suppress the amplitudes of the reflected waves in different directions, resulting in the variation of the reflection efficiency. Thus, even though identical local design steps are implemented based on the GSL, the actual performance of the local WAMs with FSI is hard to predict using the GSL.

APPENDIX C: THEORETICAL ANALYSIS OF THE FSI

To analyze the difference in FSI between air-solid and water-solid systems, we simplify and construct a coupled

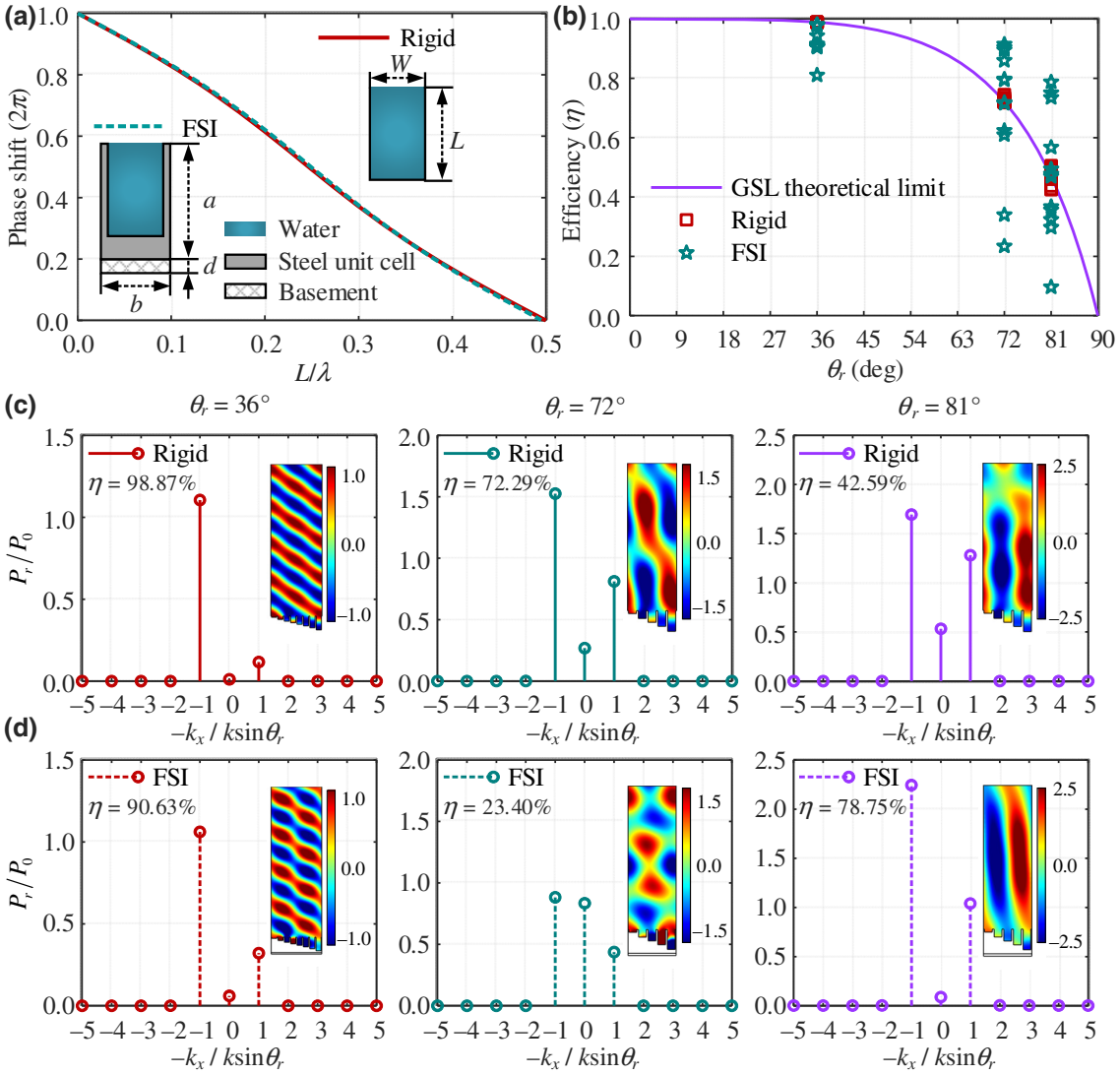

FIG. 10. Influence of FSI on the local WAM. Panel (a) shows the variation of the phase shifts of the channel-type unit cell with rigid and FSI boundaries. The reflection efficiency η of the local WAM as a function of the reflected angle θ_r is presented in (b), where the purple solid line represents the GSL theoretical efficiency limitation, and squares and stars denote the efficiencies of the local WAMs with rigid and FSI boundaries for 12 phase constants C ($\pi/6 - 2\pi$ with a step of $\pi/6$), respectively. Panels (c) and (d) show the FFT amplitudes of the reflected pressure on a transverse line located at $z = 1.5D$ as a function of $-k_x/k$ sin θ_r, which are presented to calculate the reflection efficiency of the local WAMs with rigid (c) and FSI (d) boundaries for $\theta_r = 36°$ (1st column), $\theta_r = 72°$ (2nd column) and $\theta_r = 81°$ (3rd column) at $C = 2\pi$, respectively. The solid and dashed lines represent the cases with rigid and FSI boundaries, respectively. The insets show the real parts of the reflected acoustic pressure fields within one supercell ($0 \le x \le D$ and $z \le 3D$), where D is the width of a supercell.

plate-fluid system, as shown in Fig. 11. The coupled system consists of the repetitive plate-fluid-plate sandwich model. The distance between two plates is 2δ and the thickness of a single plate is e.The interior structure between two plates is ignored, and the coupling between fluid and plate is mainly discussed. When there exists a propagation wave of angular frequency ω on one side, the acoustic pressure difference will induce the flexural vibration of the plates. Let us assume the wave numbers along the z direction in the areas II and III are k_{z_2} and k_{z_3}, respectively. Neglecting reflections on the upper and lower boundaries, the two-dimensional simple harmonic acoustic pressure fields in the areas II and III are assumed to be [37]

$$p_2(x,z) = \bar{p}_2(x) exp(j k_{z_2} z), \qquad \text{(C1-1)}$$

$$p_3(x,z) = \bar{p}_3(x) exp(j k_{z_3} z), \qquad \text{(C1-2)}$$

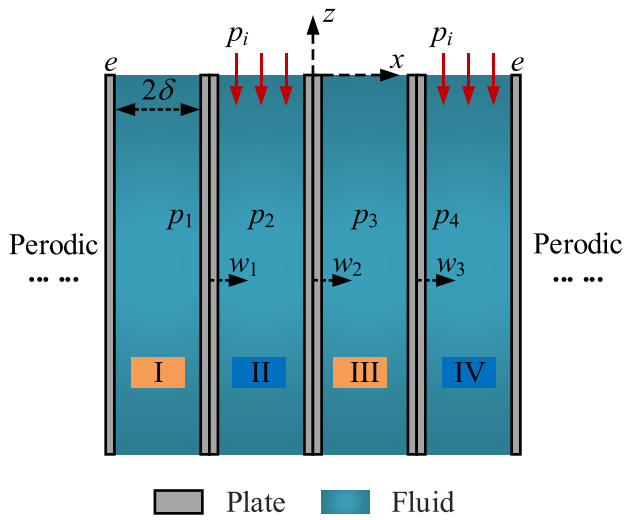

FIG. 11. Theoretical analysis on the FSI. Coupled plate-fluid layer system consists of the plate-fluid-plate sandwich model. There exists a propagation wave on one side, such as areas II and IV.

where $\bar{p}_2(x)$ and $\bar{p}_3(x)$ satisfy the acoustic wave equation

$$\frac{\partial^2 \bar{p}_2(x)}{\partial x^2} + k_{x_2}^2 \bar{p}_2(x) = 0, \tag{C2-1}$$

$$\frac{\partial^2 \bar{p}_3(x)}{\partial x^2} + k_{x_3}^2 \bar{p}_3(x) = 0. \tag{C2-2}$$

The solutions for $\bar{p}_2(x)$ and $\bar{p}_3(x)$ can be expressed as

$$\bar{p}_2(x) = A \exp[-j k_{x_2}(x + \delta + e)] + B \exp[j k_{x_2}(x + \delta + e)], \tag{C3-1}$$

$$\bar{p}_3(x) = C \exp[-j k_{x_3}(x - \delta - e)] + D \exp[j k_{x_3}(x - \delta - e)]; \tag{C3-2}$$

where $k_{x_2} = \sqrt{k^2 - k_{z_2}^2}$; $k_{x_3} = \sqrt{k^2 - k_{z_3}^2}$ with $k = \omega/c_f$ and c_f is the velocity in the fluid. According to the periodicity, acoustic pressure fields in the areas I and IV can be obtained by $p_1(x,z) = p_3(x,z)$ and $p_2(x,z) = p_4(x,z)$. Then the equations of acoustic-induced flexural vibration of the plates give [37]

$$-m_\rho \omega^2 w_1(z) + D\nabla^4 w_1(z) = p_1(x,z)|_{x=-2\delta-3e} - p_2(x,z)|_{x=-2\delta-e}, \tag{C4-1}$$

$$-m_\rho \omega^2 w_2(z) + D\nabla^4 w_2(z) = p_2(x,z)|_{x=-e} - p_3(x,z)|_{x=+e}, \tag{C4-2}$$

$$-m_\rho \omega^2 w_3(z) + D\nabla^4 w_3(z) = p_3(x,z)|_{x=2\delta+e} - p_4(x,z)|_{x=2\delta+3e}, \tag{C4-3}$$

where $w_i(z) = \bar{w}_i \exp(j K_{z_i} z), i = 1, 2, 3$ and K_{z_i} are the flexural vibration displacements and wave numbers of the three plates, respectively; $m_\rho = 2e\rho_s$ and $D = (2e)^3 E/12(1-\sigma^2)$ denote the areal density and the bending stiffness of the plates with ρ_s, E, and σ being density, elastic modulus, and Poisson's ratio of the plates, respectively. Substituting Eq. (C1) into Eq. (C4), we get

$$K_{z_1} = K_{z_2} = K_{z_3} = k_{z_2} = k_{z_3} = k_z, \tag{C5}$$

where k_z is the assumed propagation wave number in the negative z axis direction. Furthermore, the normal particle velocity boundary conditions on the surfaces of the plates give [37]

$$-j\omega w_1(z) = \frac{1}{j\omega\rho_f}\frac{\partial p_1(x,y)}{\partial x}\bigg|_{x=-2\delta-3e} = \frac{1}{j\omega\rho_f}\frac{\partial p_2(x,y)}{\partial x}\bigg|_{x=-2\delta-e}, \tag{C6-1}$$

$$-j\omega w_2(z) = \frac{1}{j\omega\rho_f}\frac{\partial p_2(x,y)}{\partial x}\bigg|_{x=-e} = \frac{1}{j\omega\rho_f}\frac{\partial p_3(x,y)}{\partial x}\bigg|_{x=+e}, \tag{C6-2}$$

$$-j\omega w_3(z) = \frac{1}{j\omega\rho_f}\frac{\partial p_3(x,y)}{\partial x}\bigg|_{x=2\delta+e} = \frac{1}{j\omega\rho_f}\frac{\partial p_4(x,y)}{\partial x}\bigg|_{x=2\delta+3e}, \tag{C6-3}$$

where ρ_f is the density of the fluid. Combining with Eqs. (C4)–(C6) and $w_1(z) = w_3(z)$, we can obtain

$$\bar{w}_1 = \bar{w}_3 = -\bar{w}_2, \tag{C7-1}$$

$$A = B = -C = -D. \tag{C7-1}$$

Finally, we can establish the dispersion relationship as

$$(1 - k_z^4/K_b^4) k_x \delta \tan(k_x \delta) - 2\rho_f \delta/m_\rho = 0, \tag{C8}$$

where $K_b = (\omega^2 m_\rho/D)^{1/4}$ is the natural flexural wave number of the plate.

To illustrate, we consider two kinds of fluids with different acoustic impedances: air and water. The material of the plates is steel. The related material parameters are listed in Table I. The wavelength λ_f is fixed at 0.15 m. Using Eq. (C8), we can solve the propagation wave number k_z of the plate-fluid-plate system. Several cases are calculated, and the normalized wave numbers (k_z/K_b) are listed

TABLE I. The corresponding material parameters.

E(GPa)	σ	ρ_s (kgm^{-3})	ρ_w (kgm^{-3})	c_w (ms^{-1})	ρ_a (kgm^{-3})	c_a (ms^{-1})
210.6	0.3	7780	1000	1500	1.21	343

TABLE II. The corresponding geometrical parameters and analytic solutions.

e	δ	k_z/K_b	
		Air	Water
$\lambda_f/20$	$\lambda_f/8$	0.9998	0.5645
$\lambda_f/30$	$\lambda_f/8$	0.9996	0.3739
$\lambda_f/40$	$\lambda_f/8$	0.9990	0.2193
$\lambda_f/40$	$\lambda_f/7$	0.9992	0.2978
$\lambda_f/40$	$\lambda_f/6$	0.9993	0.3590

in Table II. It can be noticed that all solutions of k_z for air are very close to K_b. This indicates that the motion of the plates is mainly in the form of free vibration. The FSI between the air and steel is extremely weak and has no influence on the plates. By contrast, the value of k_z/K_b for water is less than 1 and depends highly on the geometrical parameters of the plate-fluid system. This proves that when acoustic waves are propagating in water, the FSI effect can indeed induce the flexural vibration of the plates. Meanwhile, the induced vibration also interferes with acoustic pressure fields in adjacent areas in turn.

APPENDIX D: LOCALITY BETWEEN THE AIRBORNE UNIT CELLS

As a comparison, we also perform the same simulations for the airborne unit cells as for the waterborne unit cells in Figs. 3(a)–3(c). The acoustic velocity and density of the air are 343 ms^{-1} and 1.21 kgm^{-3}, respectively. The frequency is set at $f = 2.2867$ kHz to ensure the same working wavelength. All the parameters of the airborne unit cells and boundary conditions are identical to those in Figs. 3(a)–3(c). The corresponding reflected acoustic pressure fields are shown in Figs. 12(a)–12(c). The identical reflected acoustic pressure fields appear in single unit cell no. 3 in Fig. 12(a), in the homogeneous UCA of unit cell no. 3 in Fig. 12(b) and in unit cell no. 3 in the inhomogeneous UCA in Fig. 12(c). Meanwhile, the amplitudes of the reflected acoustic pressure for each unit cell in the inhomogeneous UCA in Fig. 12(c) are uniform, and are the same as those of single unit cells no. 1–5 in Fig. 12(a). This indicates that the locality between the airborne unit cells allows the single unit cell to be analyzed separately, which distinguishes this case from nonlocal interactions between the waterborne unit cells.

APPENDIX E: INFLUENCE OF MATERIAL PARAMETERS ON NONLOCAL INTERACTION

The influence of material parameters on nonlocal interaction can be characterized through the acoustic impedance of a homogenous material. In general, the characteristic acoustic impedance of a solid material for longitudinal waves can be expressed as

$$Z_p = \rho c_p = \sqrt{\rho E(1-\upsilon)/[(1+\upsilon)(1-2\upsilon)]} \propto \sqrt{\rho E} \tag{E1}$$

where c_p denotes the velocity of the longitudinal wave; and ρ, E and υ represent density, Young's modulus, and Poisson's ratio, respectively. If the acoustic impedance is large enough, the nonlocal interaction between waterborne unit cells may be neglected. To illustrate, we first consider a hypothetical material with $\rho = \zeta\rho_s$, $E = \zeta E_s$ and $\upsilon = \upsilon_s$, where ζ is the scaling factor of material parameter; and ρ_s, E_s and υ_s are density, Young's modulus and Poisson's ratio of the steel. As in Fig. 3(c), we consider an inhomogeneous UAC to examine the effect. In the calculation, the material of the basement is the same as before (steel). Figure 13(a) presents the phase shifts and reflection coefficients as functions of the scaling factor ζ for $L_1(=L_5) =$ 12 mm. The results are approximately the same as those for the unit cell with the rigid walls for $\zeta > 10^3$, where nonlocal interactions induced by the FSI can be almost neglected. However, a material with an impendence 1000 times larger than the steel can rarely be found in nature.

In addition, the variation of reflection coefficient and phase shift with Poisson's ratio ($0.01 \le \upsilon \le 0.49$) are

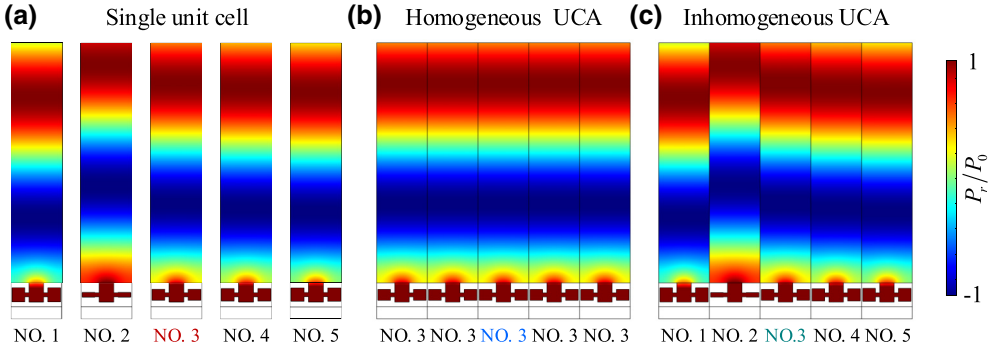

FIG. 12. Locality between the airborne unit cells. Panels (a)–(c) show the real parts of the reflected acoustic pressure fields of single unit cells no. 1–5, a homogeneous UCA of unit cell no. 3 and an inhomogeneous UCA of unit cells no. 1–5 at $f = 2.2867$ kHz, respectively, where unit cells no. 1–5 in panels (a)–(c) are selected from five unit cells in Fig. 2(b) and $P_0 = 1$ Pa.

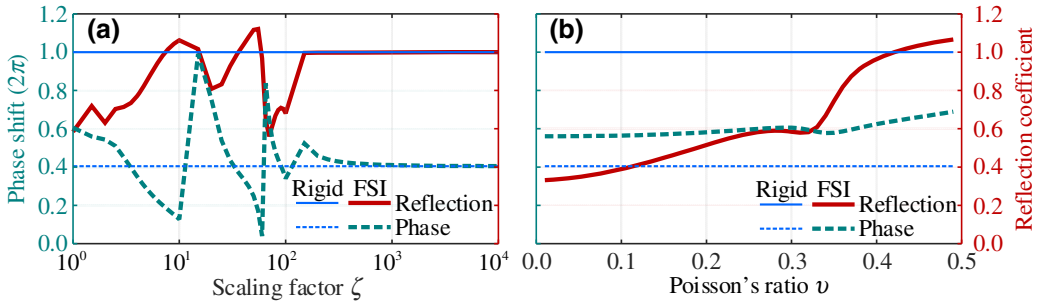

FIG. 13. Panels (a) and (b) present the phase shifts (thick dashed line) and reflection coefficients (thick solid line) of unit cell no. 3 in an inhomogeneous UCA in Fig. 3(c) as functions of scaling factor ζ and Poisson's ratio υ for $L_1(=L_5)=12$ mm, respectively. For comparison, the phase shifts and reflection coefficients for the rigid walls are also presented by thin dashed lines and thin solid lines, respectively.

given in Fig. 13(b) for $\rho=\rho_s$ and $E=E_s$. It is observed that the results deviate from those for the rigid walls. Therefore, the nonlocal effect exists for solid materials with general values of Poisson's ratio of 0–0.5. More precisely, another three solid materials, rubber, epoxy, and aluminum, are selected to investigate the influence of the material parameters on the nonlocal effect. As we have checked, the nonlocal interaction is universal for WAMs with softer (rubber or epoxy), harder (steel) or moderate (aluminum) materials.

[1] B. Assouar, B. Liang, Y. Wu, Y. Li, J. C. Cheng, and Y. Jing, Acoustic metasurfaces, Nat. Rev. Mater. **3**, 460 (2018).

[2] Y. Li, X. Jiang, R. Q. Li, B. Liang, X. Y. Zou, L. L. Yin, and J. C. Cheng, Experimental Realization of Full Control of Reflected Waves with Subwavelength Acoustic Metasurfaces, Phys. Rev. Appl. **2**, 064002 (2014).

[3] Y. Li, B. Liang, Z. M. Gu, X. Y. Zou, and J. C. Cheng, Reflected wavefront manipulation based on ultrathin planar acoustic metasurfaces, Sci. Rep. **3**, 2546 (2013).

[4] Y. Xie, W. Wang, H. Chen, A. Konneker, B.-I. Popa, and S. A. Cummer, Wavefront modulation and subwavelength diffractive acoustics with an acoustic metasurface, Nat. Commun. **5**, 5553 (2014).

[5] Y. Tian, Q. Wei, Y. Cheng, Z. Xu, and X. Liu, Broadband manipulation of acoustic wavefronts by pentamode metasurface, Appl. Phys. Lett. **107**, 221906 (2015).

[6] X. Wu, X. Xia, J. Tian, Z. Liu, and W. Wen, Broadband reflective metasurface for focusing underwater ultrasonic waves with linearly tunable focal length, Appl. Phys. Lett. **108**, 163502 (2016).

[7] Y. Chen and G. Hu, Broadband and High-Transmission Metasurface for Converting Underwater Cylindrical Waves to Plane Waves, Phys. Rev. Appl. **12**, 044046 (2019).

[8] Y. B. Jin, R. Kumar, O. Poncelet, O. Mondain-Monval, and T. Brunet, Flat acoustics with soft gradient-index metasurfaces, Nat. Commun. **10**, 6 (2019).

[9] Z. Chen, F. Yan, M. Negahban, and Z. Li, Resonator-based reflective metasurface for low-frequency underwater acoustic waves, J. Appl. Phys. **128**, 055305 (2020).

[10] J. He, X. Jiang, D. Ta, and W. Wang, Experimental demonstration of underwater ultrasound cloaking based on metagrating, Appl. Phys. Lett. **117**, 091901 (2020).

[11] L. Fan and J. Mei, Metagratings for Waterborne Sound: Various Functionalities Enabled by an Efficient Inverse-Design Approach, Phys. Rev. Appl. **14**, 044003 (2020).

[12] X. Zhang, H. Chen, Z. Zhao, A. Zhao, X. Cai, and L. Wang, Experimental demonstration of a broadband waterborne acoustic metasurface for shifting reflected waves, J. Appl. Phys. **127**, 174902 (2020).

[13] P. Li, Y. F. Chang, Q. J. Du, Z. H. Xu, M. Y. Liu, and P. Peng, Continuously tunable acoustic metasurface with rotatable anisotropic three-component resonators, Appl. Phys. Express **13**, 025507 (2020).

[14] H. Zou, P. Li, and P. Peng, An ultra-thin acoustic metasurface with multiply resonant units, Phys. Lett. A **384**, 126151 (2020).

[15] N. Yu, P. Genevet, M. A. Kats, F. Aieta, J.-P. Tetienne, F. Capasso, and Z. Gaburro, Light propagation with phase discontinuities: Generalized laws of reflection and refraction, Science **334**, 333 (2011).

[16] A. Diaz-Rubio and S. A. Tretyakov, Acoustic metasurfaces for scattering-free anomalous reflection and refraction, Phys. Rev. B **96**, 125409 (2017).

[17] J. Li, C. Shen, A. Diaz-Rubio, S. A. Tretyakov, and S. A. Cummer, Systematic design and experimental demonstration of bianisotropic metasurfaces for scattering-free manipulation of acoustic wavefronts, Nat. Commun. **9**, 1342 (2018).

[18] L. Quan and A. Alu, Passive Acoustic Metasurface with Unitary Reflection Based on Nonlocality, Phys. Rev. Appl. **11**, 054077 (2019).

[19] Y. Zhu, J. Hu, X. Fan, J. Yang, B. Liang, X. Zhu, and J. Cheng, Fine manipulation of sound via lossy metamaterials with independent and arbitrary reflection amplitude and phase, Nat. Commun. **9**, 1632 (2018).

[20] H. Ni, X. Fang, Z. Hou, Y. Li, and B. Assouar, High-efficiency anomalous splitter by acoustic meta-grating, Phys. Rev. B **100**, 104104 (2019).

[21] Z. Hou, X. Fang, Y. Li, and B. Assouar, Highly Efficient Acoustic Metagrating with Strongly Coupled Surface Grooves, Phys. Rev. Appl. **12**, 034021 (2019).

[22] Y. Fu, C. Shen, Y. Cao, L. Gao, H. Chen, C. T. Chan, S. A. Cummer, and Y. Xu, Reversal of transmission and reflection based on acoustic metagratings with integer parity design, Nat. Commun. **10**, 2326 (2019).

[23] Y. K. Chiang, S. Oberst, A. Melnikov, L. Quan, S. Marburg, A. Alu, and D. A. Powell, Reconfigurable Acoustic Metagrating for High-Efficiency Anomalous Reflection, Phys. Rev. Appl. **13**, 064067 (2020).

[24] S. W. Fan, Y. F. Zhu, L. Y. Cao, Y. F. Wang, A. Li Chen, A. Merkel, Y. S. Wang, and B. Assouar, Broadband tunable lossy metasurface with independent amplitude and phase modulations for acoustic holography, Smart Mater. Struct. **29**, 105038 (2020).

[25] Y. Fu, Y. Cao, and Y. Xu, Multifunctional reflection in acoustic metagratings with simplified design, Appl. Phys. Lett. **114**, 053502 (2019).

[26] D. Torrent, Acoustic anomalous reflectors based on diffraction grating engineering, Phys. Rev. B **98**, 060101 (2018).

[27] H. Zhu, S. Patnaik, T. F. Walsh, B. H. Jared, and F. Semperlotti, Nonlocal elastic metasurfaces: Enabling broadband wave control via intentional nonlocality, Proc. Natl. Acad. Sci. U. S. A. **117**, 26099 (2020).

[28] P. A. Cotterill, D. Nigro, I. D. Abrahams, E. Garcia-Neefjes, and W. J. Parnell, Thermo-viscous damping of acoustic waves in narrow channels: A comparison of effects in air and water, J. Acoust. Soc. Am. **144**, 3421 (2018).

[29] A. Bozhko, V. M. Garcia-Chocano, J. Sanchez-Dehesa, and A. Krokhin, Redirection of sound in straight fluid channel with elastic boundaries, Phys. Rev. B **91**, 094303 (2015).

[30] T. P. Martin, C. J. Naify, E. A. Skerritt, C. N. Layman, M. Nicholas, D. C. Calvo, G. J. Orris, D. Torrent, and J. Sanchez-Dehesa, Transparent Gradient-Index Lens for Underwater Sound Based on Phase Advance, Phys. Rev. Appl. **4**, 034003 (2015).

[31] Y.-F. Wang, S.-Y. Zhang, Y.-S. Wang, and V. Laude, Hybridization of resonant modes and Bloch waves in acoustoelastic phononic crystals, Phys. Rev. B **102**, 144303 (2020).

[32] See Supplemental Material at http://link.aps.org/supplemental/10.1103/PhysRevApplied.15.044046 for detailed geometrical parameters and thermoviscous effect on the reflection efficiency.

[33] S.-W. Fan, S.-D. Zhao, A. L. Chen, Y.-F. Wang, B. Assouar, and Y.-S. Wang, Tunable Broadband Reflective Acoustic Metasurface, Phys. Rev. Appl. **11**, 044038 (2019).

[34] B. Cheng, H. Hou, and N. Gao, An acoustic metasurface with simultaneous phase modulation and energy attenuation, Mod. Phys. Lett. B **32**, 1850276 (2018).

[35] J. C. Chen, *Acoustical Principle* (Science Press, Beijing, 2012).

[36] Y. Zhu and B. Assouar, Multifunctional acoustic metasurface based on an array of helmholtz resonators, Phys. Rev. B **99**, 174109 (2019).

[37] F. Frank and G. Paolo, *Sound and Structural Vibration: Radiation, Transmission and Response* (Elsevier, Amsterdam, 2007).